Optical coherence correlation spectroscopy (OCCS)

Stephane Broillet,[1,*] Akihiro Sato,[1] Stefan Geissbuehler,[1] Christophe Pache,[1] Arno Bouwens,[1] Theo Lasser,[1] and Marcel Leutenegger[1]

[1] *Laboratoire d'Optique Biomédicale LOB, École Polytechnique Fédérale de Lausanne, CH-1015 Lausanne, Switzerland*

[*] *stephane.broillet@epfl.ch*

Abstract: We present a new method called optical coherence correlation spectroscopy (OCCS) using nanoparticles as reporters of kinetic processes at the single particle level. OCCS is a spectral interferometry based method, thus giving simultaneous access to several sampling volumes along the optical axis. Based on an auto-correlation analysis, we extract the diffusion coefficients and concentrations of nanoparticles over a large concentration range. The cross-correlation analysis between adjacent sampling volumes allows to measure flow parameters. This shows the potential of OCCS for spatially resolved diffusion and flow measurements.

OCIS codes: (290.5850) Scattering, particles; (030.1670) Coherent optical effects; (170.4500) Optical coherence tomography.

References and links

1. D. Magde, E. Elson, and W. Webb, "Thermodynamic fluctuations in a reacting system measurement by fluorescence correlation spectroscopy," Phys. Rev. Lett. **29**, 705–708 (1972).
2. R. Rigler and E. Elson, *Fluorescence Correlation Spectroscopy: Theory and Applications* (Springer, 2001).
3. K. Hassler, P. Rigler, H. Blom, R. Rigler, J. Widengren, and T. Lasser, "Dynamic disorder in horseradish peroxidase observed with total internal reflection fluorescence correlation spectroscopy," Opt. Express **15**, 5366–5375 (2007).
4. P. Schwille, U. Haupts, S. Maiti, and W. Webb, "Molecular dynamics in living cells observed by fluorescence correlation spectroscopy with one- and two-photon excitation," Biophys. J. **77**, 2251–2265 (1999).
5. D. Schaeffel, R. Staff, H.-J. Butt, K. Landfester, D. Crespy, and K. Koynov, "Fluorescence correlation spectroscopy directly monitors coalescence during nanoparticle preparation," Nano Lett. **12**, 6012–6017 (2012).
6. K. Jaskiewicz, A. Larsen, D. Schaeffel, K. Koynov, I. Lieberwirth, G. Fytas, K. Landfester, and A. Kroeger, "Incorporation of nanoparticles into polymersomes: Size and concentration effects," ACS Nano **6**, 7254–7262 (2012).
7. P. Dittrich and P. Schwille, "Spatial two-photon fluorescence cross-correlation spectroscopy for controlling molecular transport in microfluidic structures," Anal. Chem. **74**, 4472–4479 (2002).
8. W. Schrof, J. Klingler, S. Rozouvan, and D. Horn, "Raman correlation spectroscopy: A method for studying chemical composition and dynamics of disperse systems," Phys. Rev. E. **57**, R2523–R2526 (1998).
9. T. Hellerer, A. Schiller, G. Jung, and A. Zumbusch, "Coherent anti-stokes raman scattering (cars) correlation spectroscopy," Chem. Phys. Chem. **3**, 630–633 (2002).
10. J. Cheng, E. Potma, and S. Xie, "Coherent anti-stokes raman scattering correlation spectroscopy: Probing dynamical processes with chemical selectivity," J. Phys. Chem. A **106**, 8561–8568 (2002).
11. M. Geissbuehler, Bonacina, L., V. Shcheslavskiy, N. Bocchio, S. Geissbuehler, M. Leutenegger, I. Maerki, J. Wolf, and T. Lasser, "Nonlinear correlation spectroscopy (nlcs)," Nano Lett. **12**, 1668–1672 (2012).
12. T. Liedl, S. Keller, F. Simmel, J. Radler, and W. Parak, "Fluorescent nanocrystals as colloidal probes in complex fluids measured by fluorescence correlation spectroscopy," Small **1**, 997–1003 (2005).
13. V. Octeau, L. Cognet, L. Duchesne, D. Lasne, N. Schaeffer, D. Fernig, and B. Lounis, "Photothermal absorption correlation spectroscopy," ACS Nano **3**, 345–350 (2009).

#199152 - $15.00 USD Received 6 Nov 2013; revised 19 Dec 2013; accepted 19 Dec 2013; published 7 Jan 2014

14. P. Paulo, A. Gaiduk, F. , Kulzer, S. Gabby Krens, H. Spaink, T. Schmidt, and M. Orrit, "Photothermal correlation spectroscopy of gold nanoparticles in solution," J. Phys. Chem. C **113**, 11451–11457 (2009).
15. J. Yguerabide and E. Yguerabide, "Light-scattering submicroscopic particles as highly fluorescent analogs and their use as tracer labels in clinical and biological applications i. theory," Anal. Biochem. **262**, 137–156 (1998).
16. B. Berne and R. Pecora, *Dynamic Light Scattering with Applications to Chemistry, Biology and Physics* (John Wiley and Sons, New-York, 1976).
17. D. Boas, K. Bizheva, and A. Siegel, "Using dynamic low-coherence interferometry to image brownian motion within highly scattering media," Opt. Lett. **23**, 319–321 (1998).
18. S. Dominguez-Medina, S. McDonough, P. Swanglap, C. Landes, and S. Link, "In situ measurement of bovine serum albumin interaction with gold nanospheres," Langmuir **28**, 9131–9139 (2012).
19. S. Wennmalm and J. Widengren, "Interferometry and fluorescence detection for simultaneous analysis of labeled and unlabeled nanoparticles in solution," J. Am. Chem. Soc. **134**, 19516–19519 (2012).
20. J. Chen and J. Irudayaraj, "Quantitative investigation of compartmentalized dynamics of erbb2 targeting gold nanorods in live cells by single molecule spectroscopy," ACS Nano **3**, 4071–4079 (2009).
21. M. Digman, C. Brown, P. Sengupta, P. Wiseman, A. Horwitz, and E. Gratton, "Measuring fast dynamics in solutions and cells with a laser scanning microscope," Biophys. J. **89**, 1317–1327 (2005).
22. M. Brinkmeier, K. Doerre, J. Stephan, and M. Eigen, "Two-beam cross-correlation: A method to characterize transport phenomena in micrometer-sized structures," Anal. Chem. **71**, 609–616 (1999).
23. M. Gosch, H. Blom, S. Anderegg, K. Korn, P. Thyberg, M. Wells, T. Lasser, R. Rigler, A. Magnusson, and S. Hard, "Parallel dual-color fluorescence cross-correlation spectroscopy using diffractive optical elements," J. Biomed. Opt. **10**, 054008 (2005).
24. T. Dertinger, V. Pacheco, I. Von Der Hocht, R. Hartmann, I. Gregor, and J. Enderlein, "Two-focus fluorescence correlation spectroscopy: A new tool for accurate and absolute diffusion measurements," Chem. Phys. Chem. **8**, 433–443 (2007).
25. J. Izatt and M. Choma, *Optical Coherence Tomography: Technology and Applications* (Springer Verlag, Berlin, 2008).
26. P. Schwille, "Fluorescence correlation spectroscopy and its potential for intracellular applications," Cell Biochem. Biophys. **34**, 383–408 (2001).
27. M. Leutenegger, C. Ringemann, T. Lasser, S. Hell, and C. Eggeling, "Fluorescence correlation spectroscopy with a total internal reflection fluorescence sted microscope (tirf-sted-fcs)," Opt. Express **20**, 5243–5263 (2012).
28. T. Wohland, R. Rigler, and H. Vogel, "The standard deviation in fluorescence correlation spectroscopy," Biophys. J. **80**, 2987–2999 (2001).
29. J. Kalkman, R. Sprik, and T. Van Leeuwen, "Path-length-resolved diffusive particle dynamics in spectral-domain optical coherence tomography," Phys. Rev. Lett. **105**, 198302 (2010).
30. R. A. Leitgeb, M. Villiger, A. H. Bachmann, L. Steinmann, and T. Lasser, "Extended focus depth for fourier domain optical coherence microscopy," Opt. Lett. **31**, 2450–2452 (2006).
31. M. Villiger, C. Pache, and T. Lasser, "Dark-field optical coherence microscopy," Opt. Lett. **35**, 3489–3491 (2010).
32. C. Pache, N. Bocchio, A. Bouwens, M. Villiger, C. Berclaz, J. Goulley, M. Gibson, C. Santschi, and T. Lasser, "Fast three-dimensional imaging of gold nanoparticles in living cells with photothermal optical lock-in optical coherence microscopy," Opt. Express **20**, 21385–21399 (2012).
33. M. Villiger and T. Lasser, "Image formation and tomogram reconstruction in optical coherence microscopy," J. Opt. Soc. Am. A **27**, 2216–2228 (2010).
34. M. Leutenegger, R. Rao, R. Leitgeb, and T. Lasser, "Fast focus field calculations," Opt. Express **14**, 11277–11291 (2006).
35. M. A. van Dijk, A. L. Tchebotareva, M. Orrit, M. Lippitz, S. Berciaud, D. Lasne, L. Cognet, and B. Lounis, "Absorption and scattering microscopy of single metal nanoparticles," Phys. Chem. Chem. Phys. **8**, 3486–3495 (2006).
36. A. Tcherniak, J. Ha, S. Dominguez-Medina, L. Slaughter, and S. Link, "Probing a century old prediction one plasmonic particle at a time," Nano Lett. **10**, 1398–1404 (2010).
37. N. Cheng, "Formula for the viscosity of a glycerol-water mixture," Ind. Eng. Chem. Res. **47**, 3285–3288 (2008).
38. S. Hess and W. Webb, "Focal volume optics and experimental artifacts in confocal fluorescence correlation spectroscopy," Biophys. J. **83**, 2300–2317 (2002).
39. D. Koppel, "Statistical accuracy in fluorescence correlation spectroscopy," Phys. Rev. A **10**, 1938–1945 (1974).
40. W. Wright, G. Sonek, and M. Berns, "Parametric study of the forces on microspheres held by optical tweezers," Appl. Opt. **33**, 1735–1748 (1994).
41. M. Dienerowitz, M. Mazilu, and K. Dholakia, "Optical manipulation of nanoparticles: A review," J. Nanophotonics **2**, 021875 (2008).
42. W. Singer, M. Totzeck, and H. Gross, *Handbook of Optical Systems: Vol. 2 Physical Image Formation* (Wiley-VCH Verlag GmbH & Co. KGaA, Weinheim, 2005).
43. S. Broillet, A. Sato, S. Geissbuehler, C. Pache, A. Bouwens, T. Lasser, and M. Leutenegger, "Matlab OCCS Experiment," http://lob.epfl.ch/page-103066.html.

#199152 - $15.00 USD Received 6 Nov 2013; revised 19 Dec 2013; accepted 19 Dec 2013; published 7 Jan 2014

1. Introduction

The observation of dynamic processes at the nanoscale allows the study of kinetics at the single particle level. Fluorescence Correlation Spectroscopy (FCS) [1, 2] is a widely used technique to study enzyme reaction kinetics [3] and molecular dynamics in cells [4], but also allows investigating coalescence and aggregation [5], the interaction between nanoparticles and membranes [6] or flow in micro-channels [7]. Using fluorescence as a reporter signal has a number of advantages, in particular molecular specificity, high contrast and single molecule sensitivity. However, fluorophores tend to photo-bleach, especially when observed at high illumination intensities and/or over long time periods. This typically limits the total observation time for classical FCS to a few seconds, which complicates characterizing slow processes. On the other hand, the optical emission from fluorophores saturates at high excitation intensities, which imposes constraints for the study of fast molecular processes.

Novel techniques such as Raman correlation spectroscopy (RCS) [8], coherent anti-Stokes Raman scattering correlation spectroscopy (CARSCS) [9, 10], correlation spectroscopy based on second and third harmonic non-linear light-matter interactions (NLCS) [11] and FCS on quantum dots [12] have been conceived to overcome these drawbacks. Based on the absorption properties of gold nanoparticles (NPs) and an auto-correlation analysis, photothermal correlation spectroscopy (PCS) has been demonstrated recently [13, 14]. These gold NPs are photostable and available with biocompatible surface coatings and have been proven to be alternative markers for time-lapse observations. NPs can also be detected using their light scattering properties [15]. For instance, their diffusion properties can be measured by dynamic light scattering (DLS) [16], low-coherence interferometry (LCI) [17], scattering correlation spectroscopy (SCS) [18] or scattering interference correlation spectroscopy (SICS) [19]. The luminescence properties of gold NPs can also be used to perform FCS experiments [20], overcoming the photobleaching but not the signal limitation. Whereas DLS and SICS provide good temporal resolution, they have limited spatial resolution because the long coherence length of the monochromatic illumination integrates the signal due to particle dynamics over a wide depth range. In contrast, FCS, PCS, SCS and LCI measure particle dynamics locally but need longer time spans for measuring the spatial distribution of particle dynamics in larger volumes (using for instance raster image correlation spectroscopy (RICS) [21] in the case of FCS). Dual and multiple focal FCS systems are known to measure lateral flow and diffusion [22–24] but entail a higher complexity of the optical system.

Here we introduce Optical Coherence Correlation Spectroscopy (OCCS), which exploits the backscattered light of NPs illuminated by a broadband light source. Over a large concentration range, this technique allows the extraction of the diffusion coefficient and concentration of NPs using an auto-correlation analysis. OCCS gives simultaneous access to several sampling volumes along the optical axis, which allows assessing flow parameters through cross-correlation analysis. Thus, OCCS enables spatially resolved diffusion and flow measurements.

2. Theory

2.1. Principle of OCCS

A typical OCCS experiment is shown in Fig. 1. The sample is composed of NPs diffusing in a liquid (Fig. 1(a)). The OCCS system is a low coherence interferometer that illuminates the sample with an elongated Bessel beam (Fig. 1(b)). The LCI principle allows a multitude of sampling volumes along this Bessel beam to be interrogated simultaneously, *i.e.* the total illuminated volume can be subdivided into several sampling volumes along the optical axis. The lateral extent of a single sampling volume is determined by the numerical aperture whereas the axial extent is governed by the temporal coherence of the broadband light source. The superpo-

#199152 - $15.00 USD Received 6 Nov 2013; revised 19 Dec 2013; accepted 19 Dec 2013; published 7 Jan 2014

sition of the backscattered sample field and the reference field results in a spectral interference signal which is recorded via a spectrometer (Fig. 1(c)). The acquired spectrum is then resampled at equidistant wavenumbers (λ to k mapping, Fig. 1(d)). By taking the Fourier transform of the resampled spectrum, we obtain the time-dependent signal traces extending over several sampling volumes (Fig. 1(e)). Concentration and diffusion coefficients of identical NPs are then extracted by fitting the auto-correlations of these time-dependent signals by corresponding correlation model functions (Fig. 1(f) top). Additionally, cross-correlating time traces between adjacent sampling volumes yields access to the mean transit times of NPs moving across the axially aligned sampling volumes (Fig. 1(f) bottom). OCCS correlations therefore allow assessing diffusion, concentration and directed flow along the optical axis.

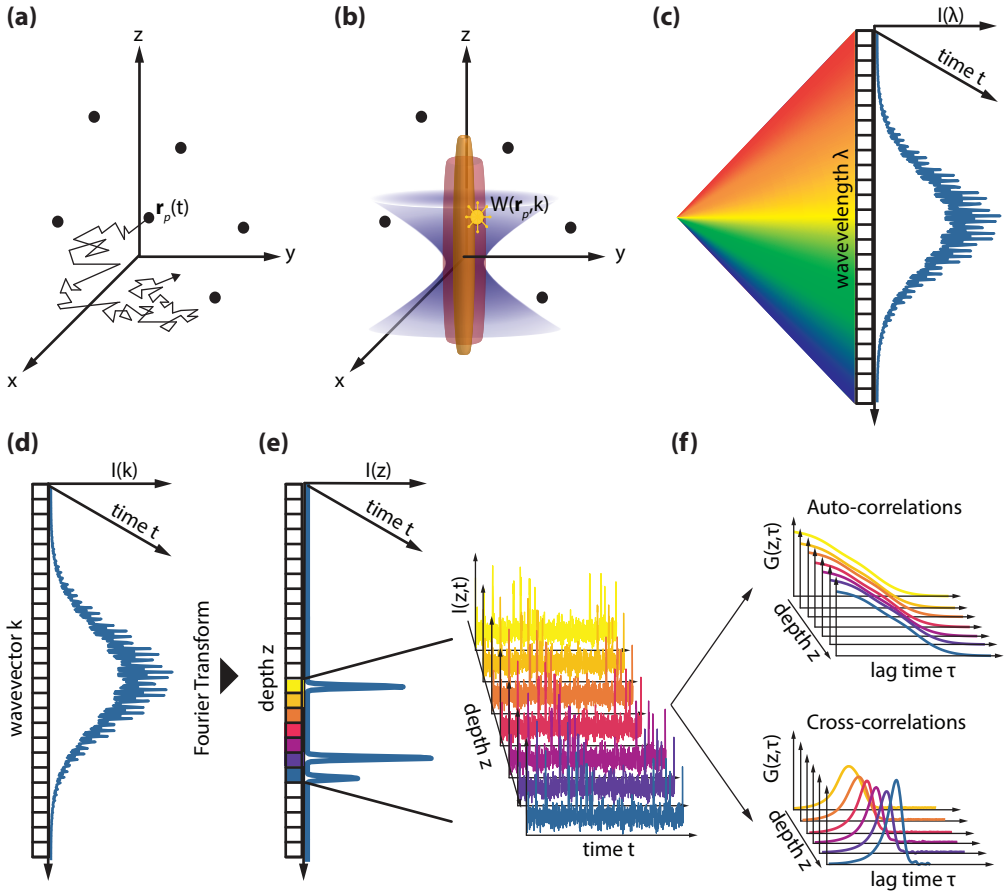

Fig. 1. A typical OCCS experiment. (a) Particles diffusing in a liquid. The trajectory $\mathbf{r}_p(t)$ of a particle is exemplified. (b) Bessel illumination of the particles and detection of the backscattered light $W(\mathbf{r}_p,k)$. (c) The interference signal generated by the backscattered sample field and the reference field is recorded via a spectrometer. (d) The sample spectrum is then re-sampled at equidistant wavenumbers (λ to k mapping) (e), and the depth profile containing a sequence of sampling volumes is extracted by computing the fast Fourier transform of the spectrum. (f) Auto-correlations of these time-dependent signals and cross-correlations of time traces between different sampling volumes are calculated.

#199152 - $15.00 USD Received 6 Nov 2013; revised 19 Dec 2013; accepted 19 Dec 2013; published 7 Jan 2014

Signal acquisition in OCCS

The spectrum of the interfering fields resulting from the superposition of the reference light and the light back-scattered from the sample is measured in OCCS. Due to the used broadband light source, OCCS has a limited temporal coherence characterized by a coherence length l_c. This allows to differentiate axial sampling volumes [25]. Supposing a Gaussian-shaped source spectrum, l_c is given as

$$l_c = \frac{2\ln(2)}{n\pi}\frac{\lambda_0^2}{\Delta\lambda}, \tag{1}$$

where n is the refractive index of the medium, λ_0 is the central source wavelength in vacuum and $\Delta\lambda$ its spectral bandwidth at full width at half-maximum (FWHM). The $1/e^2$ half width of the axial coherence gate is then $z_0 = l_c/\sqrt{2\ln(2)}$. The sampling volumes are defined as a brightness profile of $2z_0$ axial length and spaced by the center to center distance [25]

$$\Delta z = \frac{2\pi}{2\Delta k_s}, \tag{2}$$

where Δk_s is the spectral bandwidth of the spectrometer. If the available source spectrum is not fully imaged on the spectrometer, the axial resolution will be inferior to the value l_c in Eq. (1). Choosing Δk_s such that $\Delta z \lesssim l_c/2$ enables two consecutive sampling volumes to be resolved. In our case, $\Delta z = 1.66\,\mu\text{m}$ and $l_c = 3.07\,\mu\text{m}$, and $\Delta z \simeq l_c/2$.

In the plane-wave approximation, the detected signal spectrum as a function of time t at wavenumber k after mapping from λ to $k = 2\pi/\lambda$ can be written as [25]

$$\begin{aligned} I_D(k,t) = |E_r + E_s|^2 = S(k)\,|\alpha_r \exp(2\mathrm{i}kz_r) + \sum_{p=1}^{N}\alpha_p \exp(2\mathrm{i}kz_p(t))\,|^2 = \\ S(k)\left(\alpha_r^2 + \sum_{p=1}^{N}\alpha_p^2\right) + \qquad \text{(i)} \\ 2S(k)\sum_{p=1}^{N}\alpha_r\alpha_p\cos(2k(z_r - z_p(t))) + \qquad \text{(ii)} \\ 2S(k)\sum_{\substack{p=1\\q>p}}^{N}\alpha_p\alpha_q\cos(2k(z_p(t) - z_q(t)))\,, \qquad \text{(iii)} \end{aligned} \tag{3}$$

where α_p stands for the electric field reflectivity of each scatterer p and z_p their positions. α_r is the reflectivity and z_r the optical path length of the reference arm. $S(k)$ represents the power spectrum of the light source. The first term (i) is the back-reflected average power and is path-length independent. As the reference intensity is much stronger than the reflected sample intensity, subtracting the reference power spectrum eliminates the path-length independent contribution. The second term (ii) corresponds to the interference between the reference field and each scatterer's fields. This is the term of interest in OCCS because it depends on the path-length difference between the reference arm and the scatterers. The third term (iii) corresponds to the interference occurring between the fields of the scatterers. Due to the strong reference intensity, this term can be neglected. Therefore, Eq. (3) can be reduced to the second term.

Considering the case where the sample contains only scatterers of the same kind ($\alpha_p = \alpha_s\,\forall p$) and assuming only one single moving particle, the inverse Fourier transform yields the complex signal in a sampling volume V_m

$$I_{d,m}(t) = \alpha_r\alpha_s g(2n(z_1(t) - z_m)) = \alpha_r\alpha_s|g(2n(z_1(t) - z_m))|\exp(\mathrm{i}\,2nk_0(z_1(t) - z_m))\,, \tag{4}$$

#199152 - $15.00 USD Received 6 Nov 2013; revised 19 Dec 2013; accepted 19 Dec 2013; published 7 Jan 2014

where z_m is the position of the center of the sampling volume V_m and k_0 is the central wave number of the source spectrum.

We now take into account the brightness profile $W_m(\rho,z)$ of the sampling volume V_m as defined in Eq. (16). Neglecting the small phase contribution due to the radial displacement ρ, the signal $I_{\mathrm{d},m}(t)$ becomes

$$I_{\mathrm{d},m}(t) = \alpha_{\mathrm{r}}\alpha_{\mathrm{s}} W_m(\rho_1(t), z_1(t)) \exp\left(\mathrm{i}\, 2nk_0 (z_1(t) - z_m)\right). \tag{5}$$

Taking the modulus of this signal, we obtain the OCCS signal

$$I_m(t) = \alpha_{\mathrm{r}}\alpha_{\mathrm{s}} W_m(\rho_1(t), z_1(t)). \tag{6}$$

which is a similar expression as in incoherent methods like FCS. For OCCS, this expression is limited to the single particle regime ($N \ll 1$). This equation shows that I_m scales with the scattering amplitude in volume V_m because the signal is proportional to the particle electric field reflectivity α_{s}.

Auto- and cross-correlation in the single particle regime

In general, the cross-correlation function $G_{mn}(\tau)$ of the fluctuating signals $I_m(t)$ and $I_n(t)$ in the sampling volumes V_m and V_n is

$$G_{mn}(\tau) = \frac{(T-\tau)\int_0^{T-\tau} I_m(t) I_n(t+\tau)\,\mathrm{d}t}{\int_0^{T-\tau} I_m(t)\,\mathrm{d}t \int_\tau^{T} I_n(t)\,\mathrm{d}t} - 1, \tag{7}$$

where T is the measurement time and τ is the lag time. If $m = n$, $G_{mm}(\tau) = G_m(\tau)$ is the auto-correlation related to the sampling volume V_m.

In case of a directed net flow and $n \neq m$, the cross-correlations G_{mn} and G_{nm} are different. The directed flow from sampling volume V_m to V_n results in a shift of the maximum cross-correlation amplitude towards a lag time τ equal to the mean transit time τ_{mn} a NP requires to move from V_m to V_n. Hence, a flow from V_m to V_n can be evidenced by taking the difference $G_{nm} - G_{mn}$. With a net flow, this difference shows a non-zero amplitude with a maximum at $\tau = \tau_{mn}$.

In the single particle regime we estimate the shape of the auto-correlation function by [26,27]

$$G_{\mathrm{S},m}(\tau) = \frac{1}{\langle C\rangle (4\pi D\tau)^{\frac{3}{2}}} \frac{\iint W_m(\mathbf{r}) W_m(\bar{\mathbf{r}})) \exp\left(-\frac{(\mathbf{r}-\bar{\mathbf{r}})^2}{4D\tau}\right) \mathrm{d}\mathbf{r}\mathrm{d}\bar{\mathbf{r}}}{\left(\int W_m(\mathbf{r})\,\mathrm{d}\mathbf{r}\right)^2}, \tag{8}$$

where $\langle C\rangle$ is the average concentration of the particles in the sampling volume, D is the diffusion coefficient and $W(\mathbf{r})$ is the brightness profile. For a three-dimensional Gaussian volume with $1/e^2$ radii of r_0 laterally and z_0 axially, we would obtain

$$G_{\mathrm{S},m}(\tau) = \frac{\gamma}{N}\left[\left(1+\frac{\tau}{\tau_{\mathrm{xy}}}\right)\sqrt{1+\frac{\tau}{\tau_{\mathrm{z}}}}\right]^{-1}, \tag{9}$$

#199152 - $15.00 USD Received 6 Nov 2013; revised 19 Dec 2013; accepted 19 Dec 2013; published 7 Jan 2014

where N is the average number of particles in the volume and γ is the volume contrast [28]. $\tau_{xy} = r_0^2/4D$ and $\tau_z = z_0^2/4D$ are the lateral and axial diffusion times. The average number of particles N in a sampling volume is calculated using the formula

$$N = \langle C \rangle V_{\text{eff}} = \langle C \rangle \frac{\left(\int W(\mathbf{r}) \, \mathrm{d}\mathbf{r} \right)^2}{\int W^2(\mathbf{r}) \, \mathrm{d}\mathbf{r}} = \langle C \rangle \gamma^{-1} \int W(\mathbf{r}) \, \mathrm{d}\mathbf{r}, \tag{10}$$

where V_{eff} is the effective sampling volume.

This 3D Gaussian auto-correlation model has initially been used for interpreting our OCCS measurements (Fig. 2). It is obvious that this simple model is inadequate, because the shape of the measured correlation curve is significantly different from the model. As shown by the brightness profile in Fig. 4, the Gaussian approximation is only valid in the axial direction. Therefore, we applied Eq. (8) on the numerically calculated brightness profile for better estimating the shape of the auto-correlation curve. Figure 2 clearly shows the much improved match of the experimental curve and the numerical model. We attribute the residual difference to the coherent nature of OCCS that we ignored in this calculation. For a further improvement we designed a Monte Carlo based model (appendix A) taking into account the brightness $W(\mathbf{r})$ and all coherent light interactions. The simulated correlations closely approach the experimental results, which confirms that the lateral Bessel illumination profile has a significant impact on the shape of the correlation curve. The Bessel profile leads to an autocorrelation that does not monotonically decrease as the particle moves away from the center of the sampling volume. Instead, the particle transiently disappears when moving through the minima between the "Bessel" lobes. Therefore, we introduce an exponential decay term and write the auto-correlation term as

$$G_{\text{S},m}(\tau) = \frac{\gamma}{N} \left[\left(1 + \frac{\tau}{\tau_{\text{xy}}} \right) \sqrt{1 + \frac{\tau}{\tau_{\text{z}}}} \right]^{-1} \left(1 + A_{\text{b}} \exp\left(-\frac{\tau}{\tau_{\text{b}}} \right) \right) \tag{11}$$

with $\tau_{\text{b}} = r_b^2/4D$. The parameter A_{b} and the characteristic length r_b account for the radial Bessel profile. The characteristic length r_b depends on the distance between the lobes and is thus constant for a given setup. A_{b} is linked to the visibility of the Bessel side lobes. The visibility increases with the particle brightness because it depends on the signal to noise ratio (SNR). Eq. (11) closely matches the experimental correlation curve as shown in Fig. 2.

Auto-correlation in the few particles regime

We need an extended fit model when measuring at higher particle concentrations. Similarly to Eq. (5), we write the total signal of N particles within a sampling volume as

$$I_{\text{d},m}(t) = \sum_{p=1}^{N} \alpha_{\text{r}} \alpha_{\text{s}} W_m(\rho_p(t), z_p(t)) \exp\left(\mathrm{i} 2nk_0 \left(z_p(t) - z_m \right) \right). \tag{12}$$

In the image plane, the different field contributions from all particles in one sampling volume create a speckle pattern that fluctuates in time due to the particles' mutual movements (stochastic phase contributions). In a heterodyne detection, the signal of scattered light for diffusing particles decorrelates at a rate of $\exp(-q_c^2 D)$ with the scattering vector $q_c = 2nk_0$ [16]. The signal analyzed in OCCS is a product of two intensities formed in a heterodyne light scattering geometry for which Kalkman *et al.* [29] showed that it is a Lorentzian with half linewidth

#199152 - $15.00 USD Received 6 Nov 2013; revised 19 Dec 2013; accepted 19 Dec 2013; published 7 Jan 2014

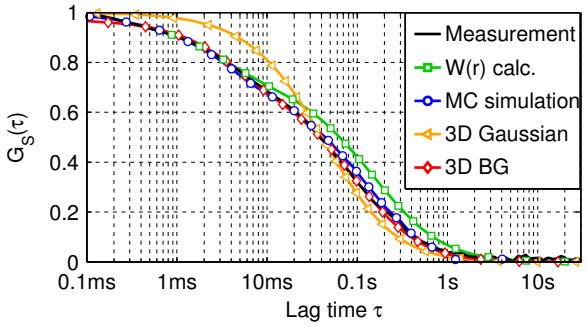

Fig. 2. Normalized OCCS curves for ⌀100nm gold NPs in water at 9.3pM in the sampling volume V_0 ($N \ll 1$). The auto-correlation curves are obtained by averaging 10 measurements. The illumination power was 2mW and each measurement lasted 100s. The measured auto-correlation is compared to different model functions: calculation from the brightness profile $W(\mathbf{r})$, from a full Monte-Carlo (MC) simulation, from an analytical model considering a 3D Gaussian volume, and from an analytical model considering a 3D Bessel-Gaussian (BG) volume.

$2q_c^2 D = 8n^2 k_0^2 D$. Integrating this coherent contribution into Eq. (11) yields

$$G_{\mathrm{F},m}(\tau) = \frac{\gamma}{N}\left[\left(1+\frac{\tau}{\tau_{\mathrm{xy}}}\right)\sqrt{1+\frac{\tau}{\tau_z}}\right]^{-1}\left(1+A_{\mathrm{b}}\exp\left(-\frac{\tau}{\tau_{\mathrm{b}}}\right)\right)\left(1+A_{\mathrm{c}}\exp\left(-\frac{\tau}{\tau_{\mathrm{c}}}\right)\right), \quad (13)$$

where

$$\tau_{\mathrm{c}} = \frac{1}{8n^2 k_0^2 D} \quad (14)$$

is the decorrelation time. A_{c} has to be proportional to N because the speckle fluctuations contrast is independent of the number of particles.

Auto-correlation in the many particles regime

As the concentration $\langle C\rangle$ increases, all terms in Eq. (13) decrease with $1/N$, *i.e.* $1/\langle C\rangle$ as in incoherent methods like FCS, but the A_c coefficient is proportionally growing with N. In consequence, the auto-correlation is dominated by the coherent particle interaction. In the many particles regime ($N \gg 1$) and because $\tau_{\mathrm{c}} \ll \tau_{\mathrm{b}}$, Eq. (13) simplifies to

$$G_{\mathrm{M},m}(\tau) = \gamma(1+A_{\mathrm{b}})\exp\left(-\frac{\tau}{\tau_{\mathrm{c}}}\right), \quad (15)$$

which corresponds to the theory for dynamic light scattering (DLS).

3. Methods

3.1. OCCS setup

Fig. 3 depicts the OCCS setup based on a Mach-Zehnder interferometer [30–32].

The broadband light source (Ti-Sa laser, Femtolasers Inc.) delivers output powers up to 400mW with a central wavelength of 790 nm and FWHM bandwidth of 130 nm. The linearly polarized output of the laser is attenuated (down to 45mW), coupled into the illumination fiber (mode field diameter of 4.2 µm, single mode polarization maintaining fiber, Fibercore

#199152 - $15.00 USD Received 6 Nov 2013; revised 19 Dec 2013; accepted 19 Dec 2013; published 7 Jan 2014

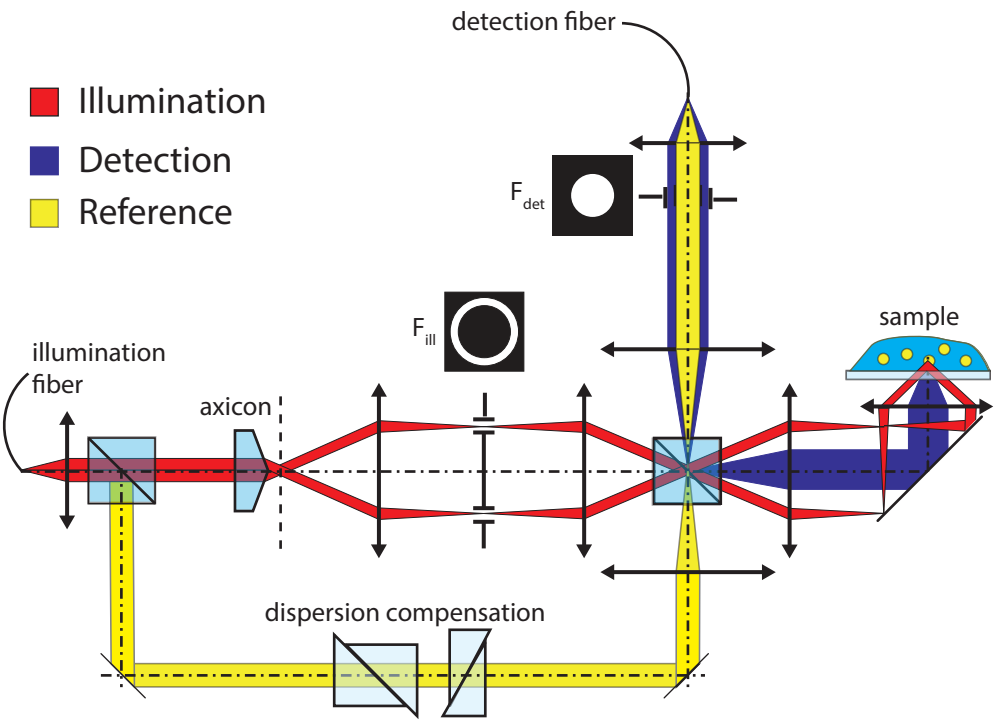

Fig. 3. Schematic of the OCCS setup. The interferometer in in a Bessel-Gauss configuration [33]: an axicon generates the Bessel beam illumination, whereas the detection mode is Gaussian. The complementary apertures F_{ill} and F_{det} are placed in conjugated planes of the objective back-aperture, ensuring the dark-field effect [31].

Ltd.) in order to adjust the power at the sample between 2-20mW (depending on the experiment). The collimated illumination is split into a reference and an illumination arm by an unpolarized beam-splitters 50/50. BK7 glass prisms located in the reference arm compensate for the dispersion mismatch due to the different optical components (objective, lenses, etc.) inside the illumination and detection arms. An axicon (176° apex angle, Del Mar Photonics Inc.) generates a radial zero-order Bessel beam, which is further imaged in the objective's focal plane by telescopes. In order to suppress residual stray light from the tip of the axicon, an illumination mask F_{ill} is placed in the intermediate focal plane of the following telescope. The epi-illuminated OCCS setup contains a 164 mm tube lens (Carl Zeiss) and a Zeiss plan apochromat water immersion objective (25×, NA 0.8) for illumination and detection. As illustrated in Fig. 3, the illumination and detection fields do not overlap in the back-focal plane of the objective. This corresponds to a dark-field configuration, which is generated by the detection aperture F_{det} conjugated to the back focal plane of the objective. Overall, this interferometer implements a so-called Bessel-Gauss configuration [33]. The complementary apertures F_{ill} and F_{det} ensure the dark-field effect. This is essential for a high SNR while measuring the weak backscattered light from NPs. The illumination field corresponds to a radial zero-order Bessel distribution in the focal plane with the first minimum located at 0.41 µm lateral radius, whereas the detection mode is Gaussian with a smaller numerical aperture (NA) of about 0.18.

The backscattered light (Fig. 1(b)) is superimposed with the reference light and focused into a single mode fiber (mode field diameter of 4.6 µm, Corning Inc.) guiding the collected light to the spectrometer (Fig. 1(c)). The customized spectrometer decomposes the input field with a

#199152 - $15.00 USD Received 6 Nov 2013; revised 19 Dec 2013; accepted 19 Dec 2013; published 7 Jan 2014

transmission grating (1200 lines/mm, Wasatch Inc.). The spectral interferogram was registered with a linear array (Atmel Aviiva M2 - 2048 pixels). The spectrum is recorded from 720nm to 860nm wavelength. The detector was set to a line rate of 10kHz with an integration time of 43 µs. The reference arm intensity is adjusted to fill about 75% of the available dynamic range of the camera. The sample spectrum is obtained by subtracting the reference spectrum from the measured spectrum. The sample spectrum is then re-sampled at equidistant wavenumbers (λ to k mapping, Fig. 1(d)) and the residual dispersion is compensated by multiplying with calibrated phase factors. The depth profile containing a sequence of sampling volumes (center to center distance of 1.66 µm in water) is then extracted by computing the fast Fourier transform (FFT) of the corrected spectrum (Fig. 1(e)). Auto-correlations of these time-dependent signals and cross-correlations of time traces between different sampling volumes are then calculated (Fig. 1(f)).

3.2. Sample preparation

Sample solutions of monodisperse polystyrene microspheres (PS MSs) with a diameter of 109nm (POLYBEAD Microspheres 0.109 µm, Polysciences, Inc.) and gold colloids (gold NPs) with diameters of 30, 50, 80 and 100nm (EM.GC30, EM.GC50, EM.GC80, EM.GC100, British Biocell International) were used. For all measurements in the single particle regime, the concentration of particles was 9.3pM, which is the supplier's given concentration of 100nm gold NPs stock solution. The solutions containing other particles were prepared by diluting an adequate volume of stock solution in ultrapure water or in glycerol. To obtain solutions of the desired concentration for the measurements in the few particles and many particles regimes, the samples were prepared using the same procedure. All sample measurements were performed in plastic wells (μ-Slide 8 well, uncoated, sterile, Ibidi GmbH) with a single well-volume of 300 µl.

3.3. Characterization of the sampling volumes

The determination of r_0, z_0, A_b and r_b is crucial for an appropriate fit model, which requires an accurate characterization of the OCCS sampling volumes. The spatial light field distribution $W(\mathbf{r}) = W(x,y,z)$ (brightness profile) was characterized by imaging individual gold NPs and polystyrene microspheres. The scattering particles were dispersed in an agarose gel with a 0.3% weight/volume ratio. We imaged individual NPs using a two axis piezoscanning stage (x-y, resolution 0.12 µm) for displacing the NPs and an illumination power of 9mW.

We compared the brightness profile measurements with ab initio calculations using the focus field calculation framework by M. Leutenegger *et al.* [34]. Based on the detection fiber specification (core diameter and NA), we calculated the conjugated Gaussian field $E_\mathrm{det}(x,y,z)$ in the object space. As OCCS is an interferometric technique, it measures the field amplitude and not the intensity. Therefore, the spatial distribution $W_m(x,y,z)$ of the detected signal in the sampling volume V_m was related to the product of the illumination field amplitude $E_\mathrm{ill}(x,y,z)$, the detection field amplitude $E_\mathrm{det}(x,y,z)$ and the coherence gate $g(2n(z-z_m))$ where z_m is the center position of sampling volume V_m.

$$W_m(x,y,z) = |E_\mathrm{ill}(x,y,z) \cdot E_\mathrm{det}(x,y,z) \cdot g(2n(z-z_m))| \tag{16}$$

Our OCCS brightness profile is rotationally symmetric around the optical axis z, such that the position can be expressed by the cylindrical coordinates (ρ,z), where $\rho = \sqrt{x^2+y^2}$. Figure 4(a) shows the measured brightness profile $W(\mathbf{r})$ in the x-y cross-section with an individual ⌀100nm gold NP, whereas the axial x-z cross-section is shown in Fig. 4(b). In Fig. 4(c) we compare the radial illumination profile (averaged on 10 particle observations) $W(\mathbf{r})$ of individual ⌀100nm, ⌀80nm, ⌀50nm, ⌀30nm gold NPs and ⌀109nm PSs MSs with the calculation (red line). As

#199152 - $15.00 USD Received 6 Nov 2013; revised 19 Dec 2013; accepted 19 Dec 2013; published 7 Jan 2014

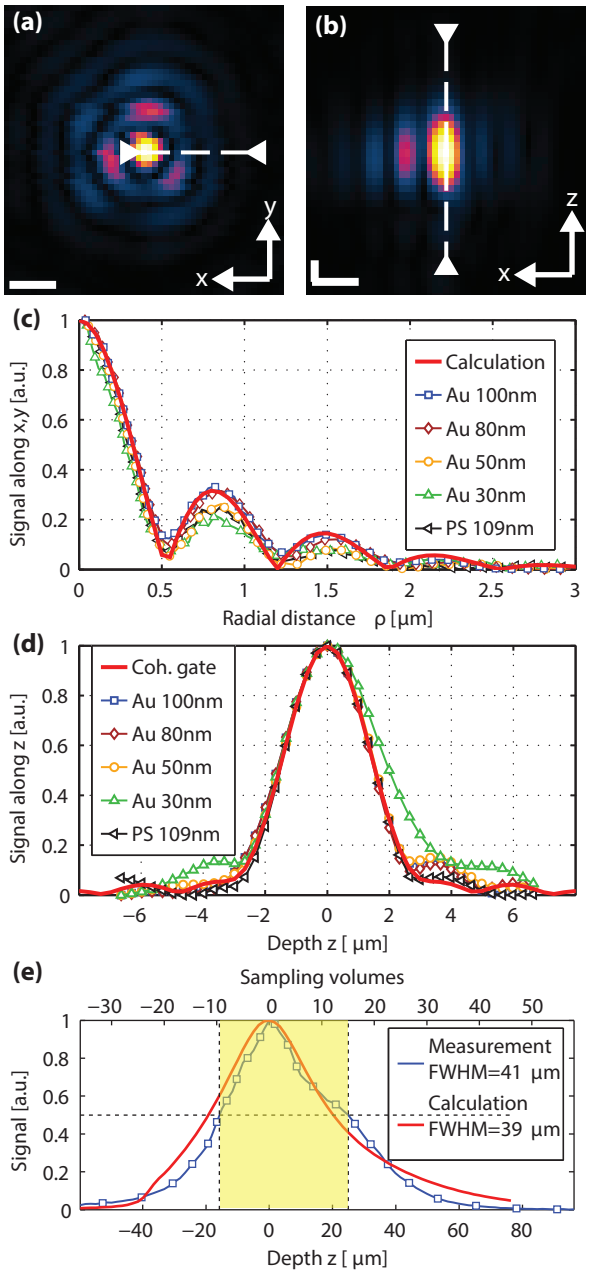

Fig. 4. Brightness profiles characterization. (a) ⌀100nm single gold NP en-face view. (b) Cross-section of the same particle along the y-axis. Scalebars: 1 μm. (c) Radial brightness profiles of ⌀100nm, ⌀80nm, ⌀50nm, ⌀30nm gold NPs and ⌀109nm PSs MSs (averaged for at least ten particles of each type) compared with calculation. (d) Axial brightness profiles of the same particles compared with the coherence gate. The ⌀30nm gold NPs axial brightness profile seems to be larger due to a lower signal-to-noise ratio (SNR). (e) Depth of field characterization with ⌀100nm gold NPs freely diffusing in water (concentration: 9.3pM; illumination power: 2mW; average on 10 measurements of 100 seconds). The useful DOF is indicated by the dashed lines showing the FWHM. V_0 corresponds to the focal sampling volume.

#199152 - $15.00 USD Received 6 Nov 2013; revised 19 Dec 2013; accepted 19 Dec 2013; published 7 Jan 2014

the particle signal decreases, so does the observed strength of the side lobes because the signal in these lobes approaches the noise level. Figure 4(d) shows the measured axial brightness profiles $W(\mathbf{r})$ compared with the coherence gate determined by the measured source spectrum $S(k)$ of our OCCS system and calculated using the Wiener-Khinchin relation. The calculated coherence gate is 3.07 µm long. We obtain a good match except for the ⌀30nm gold NPs, for which the axial brightness profile seems to be larger due to a lower signal-to-noise ratio (SNR).

The depth of field (DOF) assessment is important to evaluate the number of useful sampling volumes. We used stock solutions of ⌀100nm gold NPs (concentration of 9.3pM) freely diffusing in water, an illumination power of 2mW and measured the time-averaged signal amplitude $\langle I_m \rangle$ for the sampling volume V_m along the optical axis. Figure 4(e) compares the average DOF from 10 measurements of 100 seconds with an ab initio calculation. Within the DOF of about 40 µm FWHM, 20 sampling volumes can be observed simultaneously in axial separation steps of $\Delta z = 1.66\,\mu\text{m}$ (Eq. (2)).

3.4. Data analysis

In the single particle regime, the extent z_0 was extracted from the coherence length given by the spectrum of the light source. Figure 4(d) confirms the good agreement between the calculated and the measured axial brightness profile. The lengths r_0 and r_b were calibrated with an auto-correlation measurement of ⌀109nm polystyrene microspheres matched to Eq. (11) by using the theoretical value for the diffusion coefficient D. These characteristic lengths r_0, r_b and z_0 were then kept fixed and Eq. (11) was used to fit the auto-correlations shown in Fig. 6(a), where only A_b, N and D were free fit parameters.

A_b is obviously linked to the visibility of the side lobes as explained in section 2.3 (single particle regime). We calibrated $A_{\text{b,PS}}$ by using the ⌀109nm polystyrene microspheres. Taking the maximum signal h_s of the first side lobe with respect to the profile maximum signal in Fig. 4(c), we estimated the value $A_\text{b} = A_{\text{b,PS}} h_{\text{s,PS}}/h_\text{s}$ for other particles. We then fitted the auto-correlation curves using Eq. (11) with only N and D being free parameters. These results differ by less than 6% with respect to the previous fit with A_b as a free parameter. Considering this small difference, the fitting can be done without having to measure first the brightness profile of each particle type. However, for the smallest NPs of ⌀30nm, a correction factor has been used, as is explained in details in appendix B.

In the few particles regime, the same calibration values r_0, r_b, z_0 and $A_{\text{b,PS}}$ are used in the fit model. The free parameters are D, N and A_c. The theorical number of particles in a sampling volume is calculated from the brightness profile using Eq. (10).

4. Experimental results

4.1. Proof-of-principle experiments

It has been shown that the scattered field amplitude is proportional to the NPs volume up to diameters of 100nm [35, 36]. The expected third power dependency of the scattering signal versus NP diameter is well confirmed by our measurement as shown by the fitted trend line in Fig. 5.

In proof-of-principle experiments, we performed OCCS on freely diffusing gold NPs by varying the NP diameter and the viscosity of the solvent. Figure 6 summarizes the results of these experiments. The normalized auto-correlations of differently sized gold NPs (concentration: 9.3pM; ⌀100nm, ⌀80nm, ⌀50nm illuminated with 2mW and ⌀30nm illuminated with 8mW) are shown in Fig. 6(a). These NPs are freely diffusing in water inside the focal sampling volume V_0 (Fig. 4(e)). Extracting the diffusion coefficients is based on a straightforward fitting procedure as described in the Data Analysis section. The fit residuals are on the order of a few percent, thus confirming the quality of our method. The extracted diffusion coefficients

#199152 - $15.00 USD Received 6 Nov 2013; revised 19 Dec 2013; accepted 19 Dec 2013; published 7 Jan 2014

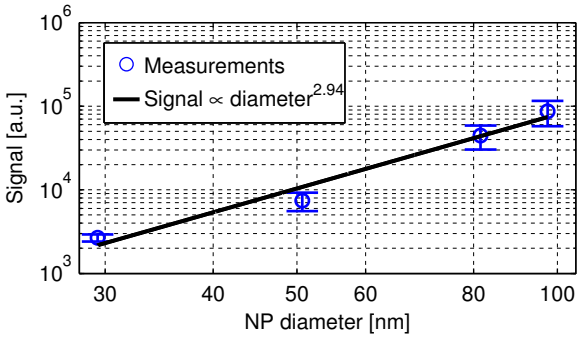

Fig. 5. OCCS signal scaling versus gold NP diameter. The OCCS signals were taken from the center of the measured brightness profiles (Fig. 4(c), illumination power of 9mW).

(Fig. 6(b)) are related by the Stokes-Einstein relation, $D = k_B T/3\pi\eta d$, where k_B is the Boltzmann constant, T the absolute temperature, η the fluid viscosity and d the particle diameter. Diffusion constants of up to 15 $\mu m^2\ s^{-1}$ were measured. In a following experiment, we varied the viscosity by measuring ⌀80nm gold NPs (illuminated with 2mW) diffusing in different glycerol/water solutions, over a range of 0% w/w up to 80% w/w of glycerol. The extracted diffusion data (Fig. 6(c)) matches well the viscosity versus glycerol concentration model according to Cheng [37].

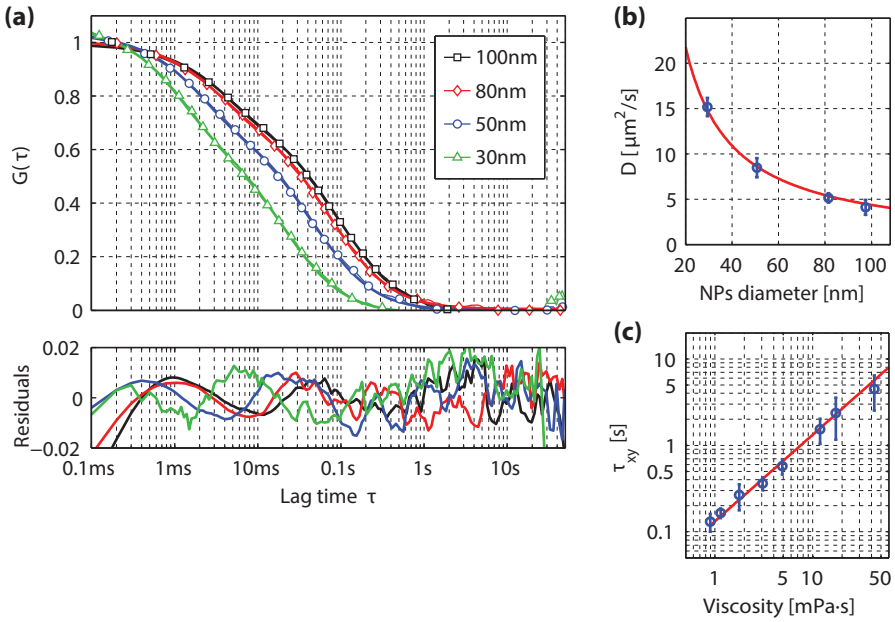

Fig. 6. (a) Normalized OCCS curves from gold NPs of different diameters in water in the single particle regime. Thin lines with markers show the average auto-correlations in V_0 of 10 measurements lasting 100 seconds each. Thick lines show the fits using Eq. (11) and the residuals. (b) The extracted diffusion coefficients compared to the theoretical values. (c) The extracted lateral diffusion time τ_{xy} of ⌀80nm gold NPs versus viscosity in various glycerin/water solutions.

So far, we introduced OCCS for the single particle regime. As OCCS is based on a coher-

#199152 - $15.00 USD Received 6 Nov 2013; revised 19 Dec 2013; accepted 19 Dec 2013; published 7 Jan 2014

ent scattering process, the coherent interaction among signals from several particles cannot be neglected if more than one particle is contained in a sampling volume. The scattered field originating from several particles results in a speckle field, *i.e.* an additional coherent contribution that is absent in intensity based methods like FCS. This speckle field fluctuates in time due to the particles' mutual movements and decorrelates at a rate of $1/8n^2\overline{k_0}^2 D$ as shown by Kalkman *et al.* [29]. Integrating this coherent contribution into Eq. (11) yields Eq. (13).

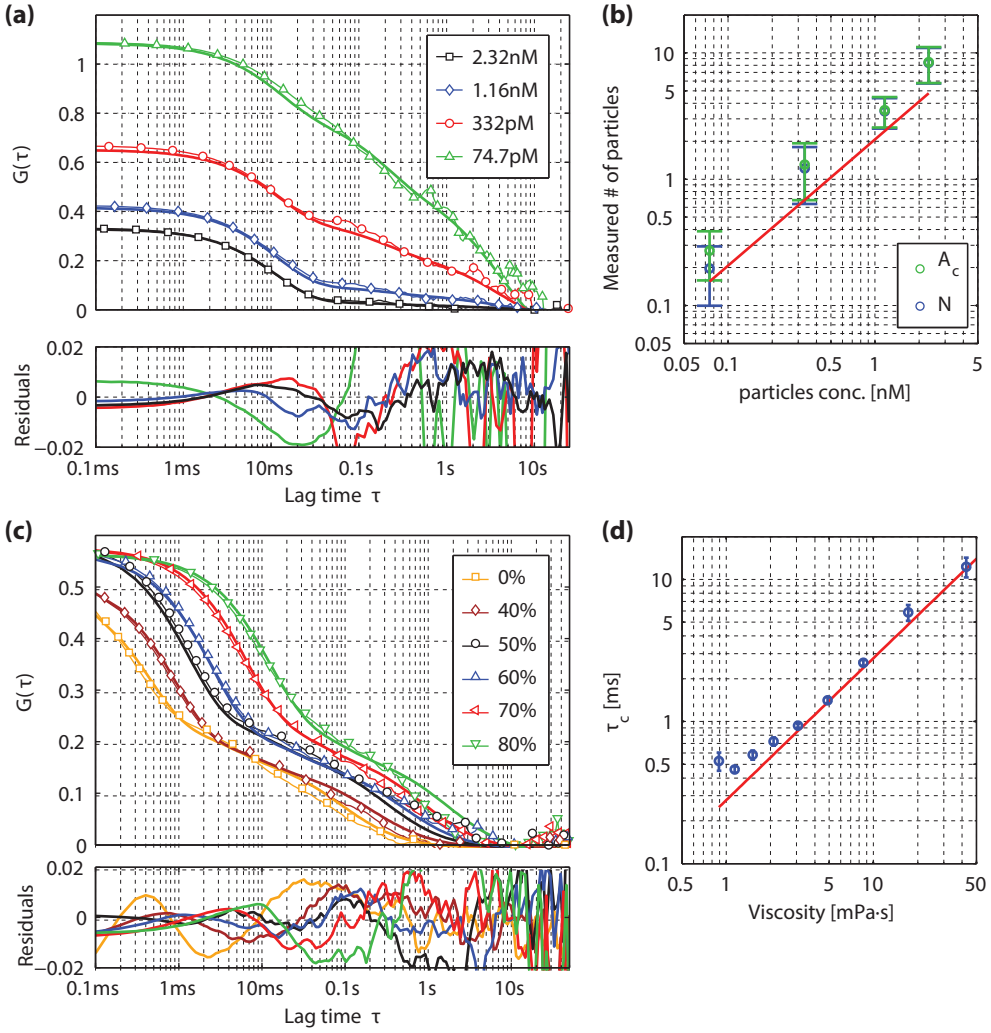

Fig. 7. (a) OCCS autocorrelations of 109nm polystyrene MSs at different concentrations in 80% glycerol/water mixtures in the focal sampling volume for a measurement of 50 seconds (thin lines with markers), along with the fit using Eq. (13) (thick lines) and the fit residuals. (b) The extracted A_c and N along with the number of particles calculated from the brightness profile (red line). Each value is averaged over 10 measurements lasting 50 seconds each. (c) OCCS autocorrelations of 109nm polystyrene MSs in glycerol/water mixtures in V_0 (thin lines with markers).Thick lines show the fits using Eq. (13). (d) The extracted τ_c as compared to the theoretical values. Each data point is averaged on 10 measurements lasting 100 seconds each.

The auto-correlations (Fig. 7(a)) were obtained by measuring ⌀109nm polystyrene micro-

#199152 - $15.00 USD Received 6 Nov 2013; revised 19 Dec 2013; accepted 19 Dec 2013; published 7 Jan 2014

spheres (PS MSs) at different concentrations in 80% glycerol/water solutions with an illumination power of 10mW. These auto-correlations have been background corrected by multiplying with $(1-\langle B\rangle/\langle I_m\rangle)^{-2}$, where B is the measured background intensity [38, 39]. The measured auto-correlations fit our phenomenological model well (Eq. (13)) as supported by the small residuals in Fig. 7(a). Figure 7(b) relates the extracted A_c and N with the number of particles estimated with Eq. (10). Concentrations below 70pM correspond to the single particle regime, for which no meaningful A_c can be extracted. According to our measurements, A_c is indeed equal to N, as has been derived by Berne and Pecora [16].

In the limit of high concentration we enter the many particles regime. As the concentration $\langle C\rangle$ increases, all contributions in Eq. (13) decrease with $1/N$, *i.e.* $1/\langle C\rangle$, but the A_c coefficient is growing proportionally with N. In consequence, the auto-correlation is dominated by the coherent particle interaction. In this regime, Eq. (13) simplifies to Eq. (15).

Figure 7(a) shows auto-correlations as a function of concentrations extending over two orders of magnitude. This demonstrates the transition from the single particle regime to the many particles regime and underlines the differences due to the coherent interactions appearing in the few particles regime. In the few particles regime, the diffusion coefficient D is also related to the decorrelation time τ_c. Figure 7(d) shows τ_c extracted from the auto-correlations (Fig. 7(c)), where the small residuals show the good agreement with our fit model. For these experiments in different glycerol/water solutions we used ⌀109nm polystyrene MSs at a concentration of 332pM (illumination power of 10mW). The background-corrected amplitudes of the auto-correlations (Fig. 7(c)) have been used to determine τ_c. The measured τ_c matches well the relation due to Cheng [37] at high viscosities (trendline), whereas deviations at low viscosity (c.f. the residuals) are mainly due to our limited sampling rate (10 kHz).

In summary, the OCCS based auto-correlation analysis applies to a wide range of particle concentrations subdivided into three regimes illustrated by Fig. 8. (i) In the single particle regime ($N \ll 1$), Eq. (11) allows assessing the mean concentration and diffusion coefficient of NPs. (ii) With increasing NP concentration (few particles regime: $N \sim 1$), the coherent interaction becomes significant and Eq. (13) adequately fits the measured auto-correlations. (iii) For high concentrations, *i.e.* the many particles regime ($N \gg 1$), the fit model simplifies to Eq. (15) and only the diffusion coefficient can be extracted.

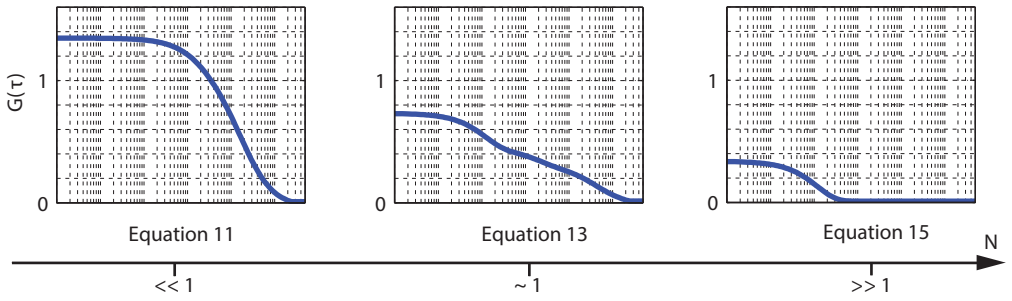

Fig. 8. The three concentrations regimes in OCCS with their corresponding fit model. Left: in the single particle regime the starting amplitude is γ/N and the decay is modeled using Eq. (11). Middle: the few particles regime is modeled according to Eq. (13). Right: the many particles regime fit model has a starting amplitude of γ and a single exponential decay according to Eq. (15).

#199152 - $15.00 USD Received 6 Nov 2013; revised 19 Dec 2013; accepted 19 Dec 2013; published 7 Jan 2014

4.2. *Multiplex advantage and cross-correlations*

OCCS has an intrinsic multiplex advantage and allows cross-correlating signals from several sampling volumes. A directed flow from sampling volume V_m to V_n results in a characteristic shift of the maximum correlation amplitude towards a lag time τ equal to the typical transit time τ_{mn} between these volumes. This peak shift is evidenced by the difference of the cross-correlation curves $\Delta G_{n,m} = G_{nm} - G_{mn}$. Obviously, no axial net flow results in $\Delta G_{n,m} = 0$.

As already observed by M. Geissbühler *et al.* [11] light scattering on NPs induces directed NPs movements. This induced net flow depends on the impinging illumination power. At low illumination power, the diffusion will dominate and the additional induced flow is insignificant (case (i)). By increasing the illumination power a notable directed flow appears (case (ii)). At low illumination power but with an additional external pump laser, the induced directed flow due to the optical forces can be easily assessed via OCCS (case (iii)).

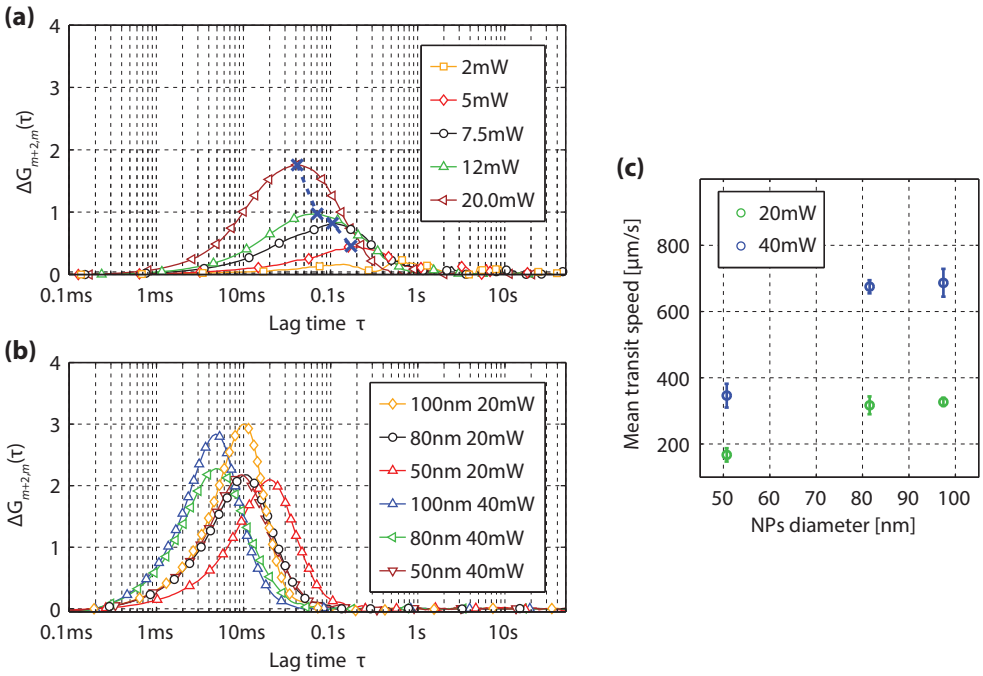

Fig. 9. (a) Cross-correlation between sampling volume V_0 and V_2, different illumination powers on a sample of ⌀100nm gold NPs. Blue cross markers indicate the mean transit time between the sampling volumes. (b) Cross-correlation between sampling volume V_0 and V_2, additional pushing laser 532nm, illumination laser at 2mW. (c) The extracted mean transition speed from the cross-correlations in (b).

Figure 9(a) shows the experimental result when measuring the OCCS signal of a ⌀100nm gold NP sample illuminated with increasing powers (2-20mW) and evaluating the cross-correlations $\Delta G_{m+2,m}$. The axial distance $2\Delta z$ is slightly greater than the coherence length l_c, minimizing the spatial overlap while increasing the sensitivity for slow axial flow. For the lowest power of 2mW negligible directed flow is perceived (case (i)), *i.e.* $\Delta G_{m+2,m} \simeq 0$. Therefore, we conclude that diffusion is the dominant process, which can be measured by OCCS. For higher illumination powers a directed flow with decreasing transit time appears (case (ii)). At powers of $\gtrsim 5mW$ the notable directed flow is due to the force equilibrium between the optical forces induced by the illumination beam and the counteracting drag force (Stokes' law) [40,41].

#199152 - $15.00 USD Received 6 Nov 2013; revised 19 Dec 2013; accepted 19 Dec 2013; published 7 Jan 2014

All measurements have been performed with V_m being the focal volume V_0 (Fig. 4(e)). Due to the Bessel illumination, the optical force varies strongly with the lateral NP position within the sampling volume, which causes a spread in transit times that is difficult to model. Therefore, we estimated the mean transit time by the lag time of $\max(\Delta G_{m+2,m})$ (blue crosses in Fig. 9(a)). Taking into account the distance $2\Delta z = 3.32\,\mu$m between the sampling volumes, a mean transit speed of 20 µm/s at 5mW illumination power and of 80 µm/s at 20mW has been measured. For all the previous concentration and diffusion measurements based on the auto-correlation analysis, we kept the illumination power small and checked for a negligible net flow ($\Delta G_{m+2,m} \simeq 0$).

To study case (iii), we used an additional laser beam at 532nm with 20mW and 40mW power to push differently sized gold NPs through the sampling volumes (2mW illumination power). This extra laser beam with a Gaussian beam shape had been focused 25 µm further away from the objective than the observation focus with an effective NA of 0.19 (source: diode pumped solid state laser, Roithner Lasertechnik, Austria). The cross-correlations differences $\Delta G_{m+2,m}$ are shown in Fig. 9(b) and the observed mean transit speeds are shown in Fig. 9(c). OCCS clearly resolves the induced flow speed exerted on identical NPs by different power levels of the extra laser source at 532 nm (see Fig. 9(c), mean transit speed between 2.0 and 2.2 times greater at 40mW than at 20mW) and, as expected, the optical forces are lower for smaller particles [41].

Figure 10 presents information on the axial flow by calculating the cross-correlations $\Delta G_{m+2,m}$ in different sampling volumes for the same three cases.

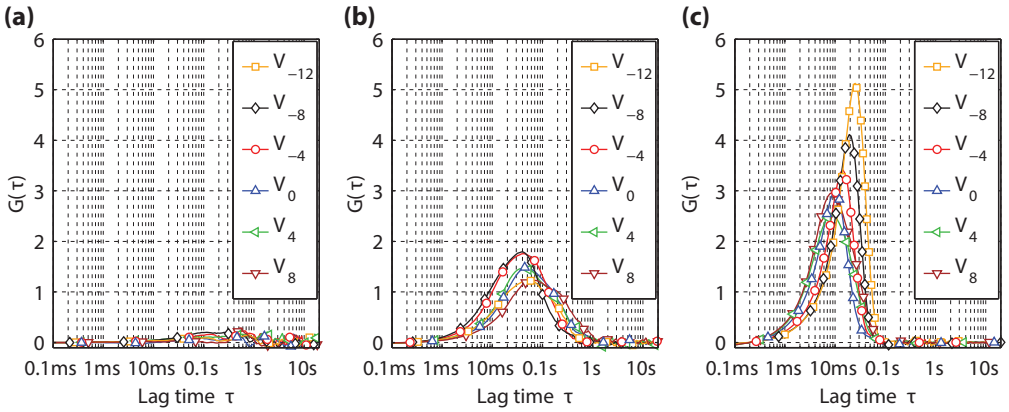

Fig. 10. Cross-correlations between sampling volumes with a sample of ⌀100nm gold NPs at a concentration of 9.3pM. (a) Illumination laser set at 2mW. (b) Illumination laser set at 20mW. (c) Illumination laser set at 2mW, while an additional laser (20mW, 532nm, Gaussian shape, NA=0.19) is used to push the particles. The legends indicate the sampling volume's relative positions from the observation focus (increasing index means further away from objective).

For case (i), Fig. 10(a) shows the results when measuring a ⌀100nm gold NP sample with an illumination power of 2mW. In that case, the cross-correlation curves do not show a clear flow signature because the diffusion is the dominant process for the NP mobility. The volumes are numbered according to Fig. 4(e). Figure 10(b) shows the resulting cross-correlations measured with ⌀100nm gold NPs in case(ii) with the illumination laser beam at a power of 20mW. Finally, in case (iii), the second laser beam was focused 25 µm further away from the objective than the observation focus. Therefore, in the sampling volumes close to the objective (negative indices), the pushing laser intensity was almost constant within a sampling volume. This led to a well defined transition time showing up a sharp peak in the cross-correlations with small lag time spread. On the other hand, closer to the focus of the green laser beam (positive indices),

#199152 - $15.00 USD Received 6 Nov 2013; revised 19 Dec 2013; accepted 19 Dec 2013; published 7 Jan 2014

the green laser beam illuminated a region smaller than the sampling volume, which led to a notable transit time spread.

5. Conclusion

In conclusion, we presented a new spectroscopic technique named Optical Coherence Correlation Spectroscopy. We used numerical simulations to estimate the performance of our method and to build an analytical model for the auto-correlation from the single particle regime up to the many particles regime. The mean NP concentration can be measured over a large range well above the single particle limit. Based on OCCS, the diffusion coefficient of gold NPs down to $\varnothing$30nm in water (approximately 15 $\mu m^2\ s^{-1}$) and in glycerol/water solutions with varying viscosities has been investigated. A key feature of OCCS is the simultaneous probing of several sampling volumes in the axial direction. The cross-correlation between signal traces originating from different volumes enabled the measurement of the mean transit speed along the axial direction (up to 700 $\mu m\ s^{-1}$ was shown). In summary, OCCS opens the door to fast 3D flow and diffusion measurements.

Appendix

A. Monte-Carlo simulation

This Monte-Carlo simulation models the essential parts of OCCS in order to investigate numerically the main concepts and to propose better fit functions for the auto- and cross-correlations. According to Fig. 1, the simulation starts by calculating random trajectories of particles due to Brownian motion within a cylindrical volume. At each time step, the back-scattered light is calculated for each particle and the summed field is superimposed with the reference field. The resulting interference spectra are then "detected" by modeling shot noise, read-out noise and truncation to discrete values. This yields the time-dependent interferograms which are then processed as real data from the spectrometer.

`occsTrajectory.m`

Single particle trajectory (free Brownian motion).

Nanoparticles trajectories

Within a cylindrical volume of lateral radius R and axial length L, we simulate the free Brownian motion of N NPs. The initial position (x,y,z) of each NP is randomly chosen in the volume by assuming a uniform distribution. The simulated measurement time T is divided in small time intervals Δt less than or equal to the sampling time of the spectrometer. The trajectory is then obtained step by step by adding normally distributed random numbers of $\Delta r = \sqrt{2D\Delta t}$ standard deviation to each coordinate of the NPs, where D are the diffusion constants of the particles.

If a particle exits the simulation volume, *i.e.* its $x^2+y^2 > R^2$ and/or $|z| > L/2$, its position is reset randomly with a uniform distribution on the surface of the cylindrical volume. Therefore, the particle concentration in the entire volume is kept constant, whereas the local concentration varies due to Brownian motion of the particles. The random reseting of the position avoids long-term correlations between particles leaving and entering the simulation volume.

`occsBrightness.m`

Approximative OCCS brightness profile modeling a Bessel illumination profile and a Gaussian detection profile.

#199152 - $15.00 USD Received 6 Nov 2013; revised 19 Dec 2013; accepted 19 Dec 2013; published 7 Jan 2014

Brightness profile

The brightness profile of the back-scattered light by a small particle can be approximated by the scalar product of the illumination field amplitude $E_{\mathrm{ill}}(\rho,z,k)$ and the field amplitude $E_{\mathrm{det}}(\rho,z,k)$ detected by the single-mode fiber. $k = 2\pi n/\lambda$ is the wave vector inside the sample medium with refractive index n. We assume rotational symmetry around the optical axis z, and use cylindrical coordinates (ρ,z), where $\rho = \sqrt{x^2+y^2}$. Within the illumination and detection volume, the light keeps to a large extent its linear polarization, such that the polarization of the field can be neglected. The amplitude $W(\rho,z,k) = E_{\mathrm{ill}}(\rho,z,k)E_{\mathrm{det}}(\rho,z,k)$ approximates then the detected amplitude spectrum of a point-like scatterer at the position (ρ,z), that is the brightness profile for detecting a small particle at the wavenumber k.

The lateral illumination profile is modeled as a zero-order Bessel profile $J_0(2.404k\rho/k_{\mathrm{c}}\rho_0)$ of the first kind, where $\rho_0 = 410\mathrm{nm}$ is the radius of the first Bessel zero at the central wave vector $k_{\mathrm{c}} = nk_0 = 2\pi n/\lambda_0$. The axial illumination profile is given by the axial spread z_0 as determined by the waist of the Gaussian amplitude profile on the conical wavefront. The maximum field shall be reached at $z = 0$, which yields the illumination profile

$$E_{\mathrm{ill}}(\rho,z,k) = J_0\left(\frac{2.404k\rho}{k_{\mathrm{c}}\rho_0}\right)\max\left(0,v(z)\right)\exp\left(\frac{1-v^2(z)}{2} - \mathrm{i}\,kz\cos\theta\right), \tag{17}$$

where $v(z) = 1+\sqrt{2}z/z_0$. The cone semi-angle of the illumination beam is θ, which is given by $\sin\theta = 2.404/k_{\mathrm{c}}\rho_0$.

For negative $v(z)$, the axial field is null because the illumination cone does not reach the optical axis. The present approximation does not model the non-overlap zone for $v(z) < 0$ in which the beam profile is a converging half-Gaussian ring. For $0 < v(z) \lesssim 0.2$, the calculated beam profile approaches the real beam profile and becomes sufficiently accurate for $v(z) \gtrsim 0.2$. We observe this range by limiting the calculations to the FWHM of the axial profile, that is to the range $-0.481z_0 \lesssim z \lesssim 0.652z_0$.

The Gaussian detection profile is accurately calculated by the well-known formula for the propagation of the amplitude in a Gaussian beam [42].

$$E_{\mathrm{det}}(\rho,z,k) = \frac{w(0,k)}{w(z,k)}\exp\left(\frac{-\rho^2}{w^2(z,k)} + \mathrm{i}\arctan\left(\frac{z}{Z(k)}\right) - \mathrm{i}\,k\frac{\rho^2}{2R(z,k)} - ikz\right) \tag{18}$$

$R(z,k)$ is the radius of wavefront curvature, $w(z,k)$ is the beam waist and $Z(k)$ is the Rayleigh length.

$$\begin{aligned} R(z,k) &= z\left(1+\frac{Z^2(k)}{z^2}\right) \\ w(z,k) &= \frac{w_0k_{\mathrm{c}}}{k}\sqrt{1+\frac{z^2}{Z^2(k)}} \\ Z(k) &= \frac{w_0^2k_{\mathrm{c}}^2}{2k} \end{aligned} \tag{19}$$

With good approximation, the single-mode fibers serving as illumination source and detection pinhole have non-dispersive numerical apertures (NA). Also, the axicon and lenses show only a small dispersion of the refraction index. Neglecting this material dispersion, the Gaussian beam waist $w(0,k)$ and the Bessel beam waist ρ_0 scale with the wavelength (factor k_{c}/k) and need only be given for the central wave vector k_{c}.

In order to speed up the simulation, we further approximated the brightness profile by splitting off the wavelength dependency and by neglecting small phase contributions in the Gaussian

#199152 - $15.00 USD Received 6 Nov 2013; revised 19 Dec 2013; accepted 19 Dec 2013; published 7 Jan 2014

detection mode. Using these simplified Eq. (17) and Eq. (18), we approximated the brightness profile by the amplitude for $k = k_c$ multiplied by the axial phase factor:

$$W(\rho, z, k) \approx J_0\left(\frac{2.404\rho}{\rho_0}\right) \max(0, v(z)) \exp\left(\frac{1-v^2(z)}{2}\right) \times \frac{w(0,k_c)}{w(z,k_c)} \exp\left(\frac{-\rho^2}{w^2(z,k_c)}\right) \times \exp\left(-ikz(1+cos\theta)\right). \tag{20}$$

We calculate the axial phase factor just upon integration over all scatterers in the `occsInterferogram` function. This requires only little memory such that multi-threaded calculations on graphics cards can be used.

occsInterferogram.m

Interference spectrum intensity for scattered field(s).

occsDetect.m

Detected intensity converted to digital values.

Detected interferogram

The signal intensity on the spectrometer is given by the interference between all field contributions $E_s(k)$ back-scattered from the particles and the reference field $E_r = \exp(2i z_r k)$. The sample field is given by

$$E_s(k) = \sum_{p=1}^{N} \alpha_p W(\rho_p, z_p, k), \tag{21}$$

where we assume that the particles reflectivity α_p is approximately constant across the source spectrum. The signal on the spectrometer is then

$$I(k) = S(k)|E_r(k) + E_s(k)|^2, \tag{22}$$

where $S(k)$ is the intensity spectrum of the source. The source's spectral power is expressed in photons per detection interval per pixel (spectral channel). Hence, $I(k)$ yields the number of photons received during the exposure time by each detector pixel. The detector converts these photons in digital values. Firstly, shot noise is applied to the signal by drawing random numbers from a Poisson distribution with average values $I(k)$. Next, these detected photon numbers are scaled by the detector sensitivity s and an eventual bias (dark current, offset o) is added. Finally, Gaussian read noise is added (standard deviation σ) and the result is rounded and limited to the numeric range of the detector.

$$I_D(k) = [s\,\text{poissrnd}(I(k)) + o + \text{normrnd}(0,\sigma)] \in [0, 2^{\text{bits}} - 1] \tag{23}$$

occsTomogram.m

Tomogram amplitude $|A(z)|$ from interference spectrum $I_D(k)$.

Tomogram amplitude

From here on, the simulated interference spectra are processed in the same way as the measurements. First, the average spectrum $\bar{I}_D(k)$ (background and reference spectrum) is subtracted and the spectrum is interpolated to an equidistant wavenumber sampling. Then, the fast Fourier transform $A(z) = \mathscr{F}^{-1}(I_D(k) - \bar{I}_D(k))$ is calculated. The resulting tomogram is cropped to the region of interest (ROI) and only the tomogram amplitude $|A(z \in \text{ROI})|$ is retained.

#199152 - $15.00 USD Received 6 Nov 2013; revised 19 Dec 2013; accepted 19 Dec 2013; published 7 Jan 2014

B. Data analysis

For the smallest NPs of ⌀30nm, the low SNR led to a low visibility of the lateral side lobes. In this case, the value of the diffusion coefficient D seemed to increase. We investigated if the Monte-Carlo simulation could reproduce this effect. For this purpose, we simulated two kinds of particles: both had the diffusion coefficient of the ⌀100nm gold NPs. One kind was given the brightness of ⌀100nm gold NPs with an illumination power of 2mW, while the other was given the brightness of the ⌀30nm gold NPs with an illumination power of 8mW as used in the experiment. This way, we eliminated the influence of the diffusion coefficient when comparing the effect of the SNR, that is the NP brightness. The Monte-Carlo simulated auto-correlation curves for the sampling volume V_0 are shown in Fig. 11 and were fitted using Eq. (11) with r_0, A_b and N as free parameters.

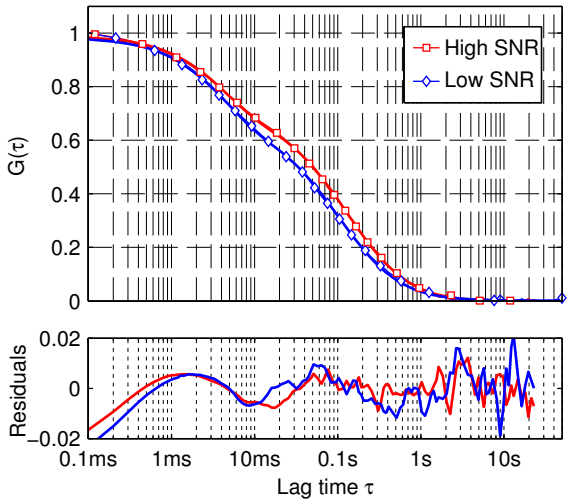

Fig. 11. Monte-Carlo simulation with two kinds of ⌀100nm NPs that were given the brightnesses of ⌀100nm and ⌀30nm gold NPs, which modeled high and low SNR, respectively, along with fits (thick lines).

It turned out that dim NPs seem to move faster. We interpret this finding as an apparent decrease of the parameter r_0 for low SNR. Because we set the brightness of the low SNR particles at the same value as the ⌀30nm gold NPs in our measurements, we could use the ratio (0.84) between the r_0 values of the two simulated curves in Fig. 11 to fit the auto-correlation curves of the measurements of the ⌀30nm gold NPs.

Supporting information

A Matlab implementation of the algorithm developed here can be downloaded from our website [43].

Acknowledgments

We acknowledge funding by the Swiss National Foundation (grant 205321L_135353).